Applied Physics A (2024) 130:507
https://doi.org/10.1007/s00339-024-07649-7

Unraveling the influence of donor defects on high-temperature ferromagnetism and dielectric properties in (Mn, Co) doped ZnO nanoparticles

Wafa Gul[1] · Sadaf Qaseem[2] · Zuhoor Elahi[1,2] · M. Naeem[2] · M. Ikram[3]

Received: 27 December 2023 / Accepted: 7 June 2024 / Published online: 21 June 2024
© The Author(s), under exclusive licence to Springer-Verlag GmbH Germany, part of Springer Nature 2024

Abstract

ZnO and $Zn_{0.98}Mn_{0.02}Co_xO$ ($0.00 \leq x \leq 0.025$) nanoparticles were synthesized via the sol-gel method and subjected to a comprehensive analysis of their structural, electronic, morphological, dielectric, and magnetic properties. X-ray diffraction (XRD) confirmed the presence of a single-phase hexagonal ZnO structure, while transmission electron microscopy (TEM) revealed spherical particles with minor facets, consistent with high-resolution TEM (HR-TEM) data. X-ray photoemission spectroscopy (XPS) analysis demonstrated successful Co and Mn incorporation into the ZnO lattice without secondary phases. Dielectric properties were investigated via impedance spectroscopy, with results interpreted using the Maxwell-Wagner model to elucidate interfacial polarization mechanisms. Magnetic measurements revealed complex interactions in Mn-doped ZnO nanoparticles, including ferromagnetic, paramagnetic, and antiferromagnetic behaviors. However, the introduction of Co as a co-dopant stabilized the ferromagnetic moment in the (Zn, Mn)O system, attributed to the presence of sufficient oxygen vacancies. Notably, our findings provide strong evidence for defect-mediated ferromagnetism in (Mn, Co) co-doped ZnO nanoparticles, contributing to our understanding of magnetic phenomena in nanomaterials.

Keywords (Mn, Co) co-doped ZnO · Mixed magnetic phases · Defect mediated FM · DMS

1 Introduction

Spintronics, a rapidly advancing field, focuses on manipulating the spin degree of freedom in magnetic semiconductors. Many experts believe that the 21st century will be marked as the era of spintronics, especially following the great achievement of developing the first spintronic device for quantum computing [1]. This technology holds great promise for revolutionizing electronic devices and data storage capabilities [2]. Diluted magnetic semiconductors (DMS) are central to spintronics devices, where the presence of spin-polarized electrons within a magnetic semiconductor lattice plays a crucial role. Among various DMS materials, ZnO doped with transition metals such as Fe, Co, and Mn has emerged as a particularly promising candidate for high-quality DMS applications. Significant progress has been made in the theoretical understanding of DMS, with Dietl et al. proposing a pioneering model that utilizes the well-established Zener model within a zinc-blend matrix. Their calculations indicated a Curie temperature slightly exceeding 100 K [3]. In recent years, ZnO nanoparticles doped with both Co^{2+} and Mn^{2+} ions have gained considerable attention [4]. However, despite extensive research, the stabilization mechanisms underlying the ferromagnetic moment in these systems remain a topic of intense debate [5–7]. The origin and nature of the ferromagnetic moment have yet to be conclusively elucidated. Some studies attribute variations in the ferromagnetic moment to the presence of secondary phases comprising Co and Mn [8, 9]. Conversely, alternative explanations propose that alterations in the oxidation states of transition metals, the presence of anion vacancies, and the exchange interaction of specific

✉ M. Naeem
naeem.khan@uok.edu.pk

1 Department of Physics and Astronomy, University of Southern Mississippi, Hattiesburg, USA

2 Department of Physics, University of Karachi, Karachi, Pakistan

3 Department of Physics, Hazara University, Mansehra, Pakistan

Content courtesy of Springer Nature, terms of use apply. Rights reserved.

localized defects with local spin-polarized electrons contribute to the observed variations in the magnetic moment [10]. In line with this, Wojnarowicz et al. postulated that matching the oxidation state of the host (Zn^{2+}) with that of the transition metal dopants (Co^{2+} or Mn^{2+}) results in a combination of predominantly paramagnetic behavior and some antiferromagnetic interactions [11]. Given the existing huge of literature highlighting the coexistence of paramagnetic and ferromagnetic moments, an in-depth investigation of the behavior of Co doping in a weakly ferromagnetic ZnMnO matrix would be highly valuable. Previous studies have indicated that the stabilization of the ferromagnetic moment in Co-doped ZnO typically necessitates an n-type environment, while Mn-doped ZnO tends to favor a p-type environment. Consequently, exploring the consequences of Co doping in a ferromagnetic n-type Mn-doped ZnO system would yield particularly intriguing insights.

2 Experiment

The synthesis of pure ZnO and co-doped ZnO nanoparticles ($Zn_{0.98}Mn_{0.02}Co_xO$, where $0.00 \leq x \leq 0.030$) was conducted via the sol-gel technique [8]. $Zn(NO_3)_2 \cdot 6\ H_2O$, $Co(NO_3)_2 \cdot 6\ H_2O$, $Mn(NO_3)_2 \cdot 4\ H_2O$, and NaOH were utilized as precursors. In the initial step, two aqueous ethanol solutions of 0.5 M $Zn(NO_3)_2 \cdot 6\ H_2O$ and 0.9 M NaOH were prepared under magnetic stirring for a duration of two hours. The 0.9 M NaOH solution was then added while maintaining high-speed constant stirring. The resulting solution was allowed to settle overnight under ambient conditions, and the precipitate was separated via centrifugation at 4000 rpm. The obtained precipitates underwent three rounds of washing with absolute ethanol and deionized water before being dried in an oven at approximately 60 °C for 48 h. Subsequently, the dried ZnO nanoparticles were annealed at 600 °C for six hours. In the text, the pure ZnO nanoparticles are denoted as Z, while the co-doped ZnO nanoparticles with x values of 0.000, 0.010, 0.015, 0.02, 0.025, and 0.030 are referred to as ZM, ZMC1, ZMC2, ZMC3, ZMC4, and ZMC5 respectively. All samples were used as powder form. X-ray diffraction (XRD) measurements employing Cu Ka radiation ($\lambda = 1.5405$ Å) were conducted to determine the presence of a single phase and perform structural analysis. Transmission electron microscopy (TEM) and high-resolution transmission electron microscopy (HR-TEM) techniques were employed to examine the morphology, size, and interplanar spacing. To confirm the absence of secondary phases such as metallic Co, Co_2O_3, MnO, etc., which may not be detectable using XRD alone, x-ray photoemission spectroscopy (XPS) measurements were carried out. The XPS analysis was conducted utilizing the ESCA200 spectrometer within an ultra-high vacuum environment, boasting a base pressure of 10^{-10} mbar. Equipped within the measurement chamber is a monochromatic Al (Kα) X-ray source, generating photons with an energy of 1486.6 eV. Experimental parameters were configured to maintain a full width at half maximum of 0.65 eV for the clean Au 4f7/2 line. Spectra were acquired with a photoelectron take-off angle set to normal emission at room temperature. Binding energies were determined in reference to the Fermi level, with a precision of ±0.1 eV. Dielectric measurements were performed within a frequency range of 40 Hz to 10^6 Hz using a Micro AUTOLAB/FRA instrument. Magnetization measurements as a function of temperature and magnetic field were conducted using a physical property measurement system.

3 Results and discussion

The XRD patterns of nanoparticles are shown in Fig. 1. X-ray diffraction patterns indicate that the synthesized nanoparticles are in good crystallinity. The major peaks are observed at the angles 31.8°, 34.5°, and 36.3° corresponding to the lattice planes of (100), (002), and (101) respectively. These crystalline planes are well matched with the standards JCPDS file number 36-1451 for zinc oxide nanoparticles. Compared with the standard XRD pattern, it was found that our synthesized ZnO and co-doped nanoparticles have a Wurtzite structure. The average values of the interplanar spacing are found to be 2.82, 2.60, and 2.47 Å corresponding to (100), (002), and (101) respectively. The ionic radii of dopants (Mn/Co) are different from Zn ion, thus a minor change in the peak broadening (Full width at half maximum (FWHM)) of XRD is expected. The change in FWHM is a result of both crystallite size and strain produced by the dopants and defects. The former was calculated by Debye – Scherrer's formula whereas the latter was calculated by Williamson-Hall's approach. The following is the Debye-Scherrer formula.

$$D_{(hkl)} = \frac{k\lambda}{\beta \cos\theta}$$

Where $D_{(hkl)}$ is the crystallite size, k is the shape factor having a value equal to 0.919, and β is the FWHM in radians. θ is the Bragg angle. The average value of crystallite sizes of ZnO and $Zn_{0.98}Mn_{0.02}O$ nanoparticles are estimated as 38 nm and it is found to be decreased with increasing Co concentration given in Table 1. The decreasing trend in crystallite size can be ascribed to the distortion in the lattice by dopants, which decrease the nucleation and subsequent growth rate of nanoparticles. The same results have also been reported in the literature [12] Fig. 2.

Content courtesy of Springer Nature, terms of use apply. Rights reserved.

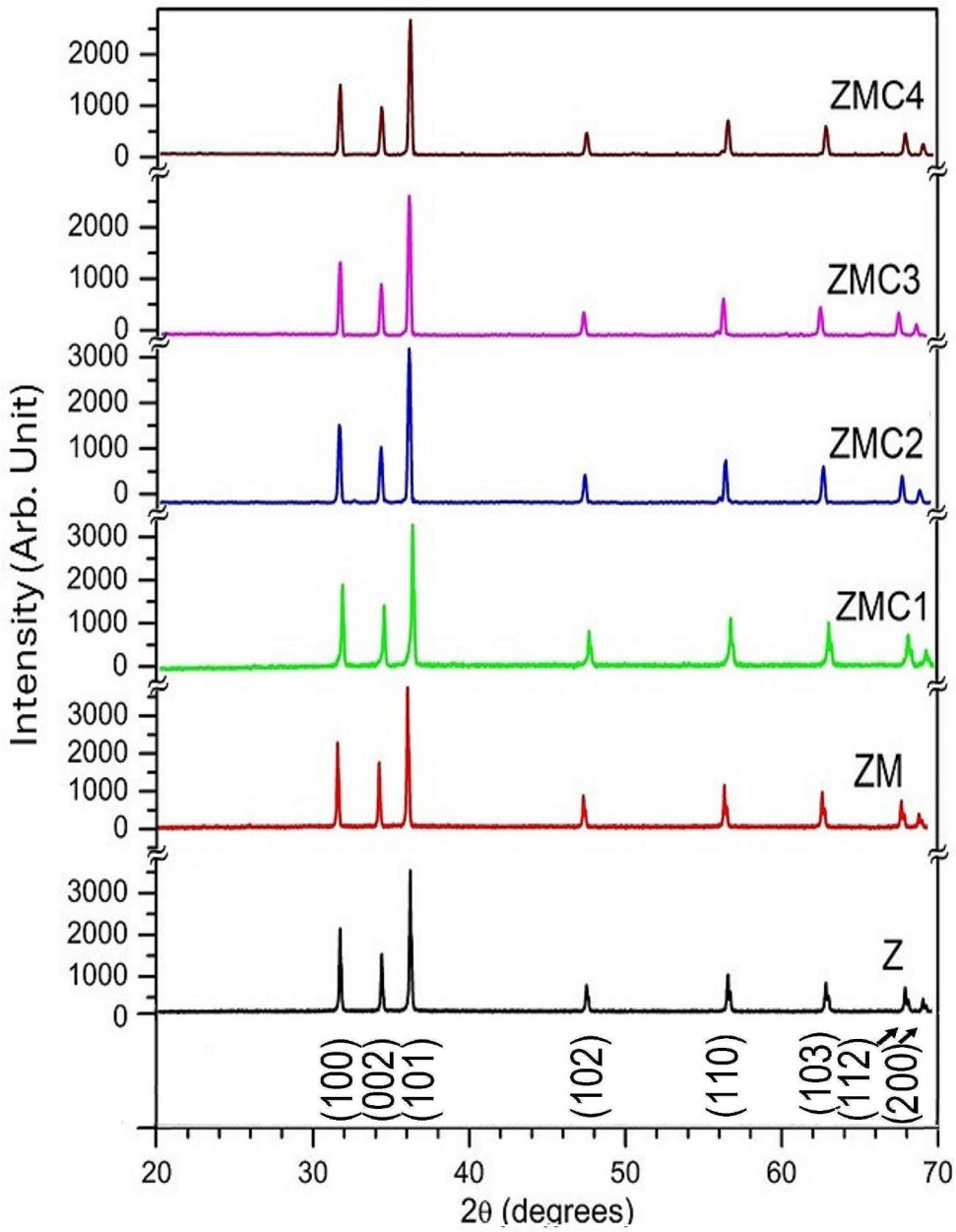

Fig. 1 XRD Patterns of bare and $Zn_{0.98}Mn_{0.02}Co_xO$ $(0.00 \leq x \leq 0.025)$ nanoparticles

Table 1 Crystallite size calculated by Scherrer, W-H approach and TEM images

Comparison of particle size: scherrer method and WH approach				
Sample code	Scherrer method	Williamson-hall approach		Tem
	Size (nm)	Size (nm)	Strain ($\times 10^{-3}$)	Size (nm)
Z	37	34	0.51	33
ZM	38	31	0.53	32
ZMC1	35	29	0.57	29
ZMC2	32	26	0.59	26
ZMC3	29	24	0.63	23
ZMC4	26	21	0.65	21

The contribution of the strain to the crystallite size can also be calculated by the Williamson-Hall approach.

$$\beta_{(hkl)} \cos\theta = \frac{k\lambda}{D_{(hkl)}} + 4\epsilon \sin\theta$$

Where $D_{(hkl)}$ is the crystallite size, β is the FWHM in radians, θ is the Bragg angle, ε is the strain. In this equation, known as the uniform deformation model (UDM), we consider a crystal is isotropic in nature, and strain is uniformly distributed in all directions. In order to calculate the crystallite size and strain, a plot is drawn between 4sin θ (on the horizontal axis) and β_{hkl} cos θ (on the vertical axis) for all diffraction

Content courtesy of Springer Nature, terms of use apply. Rights reserved.

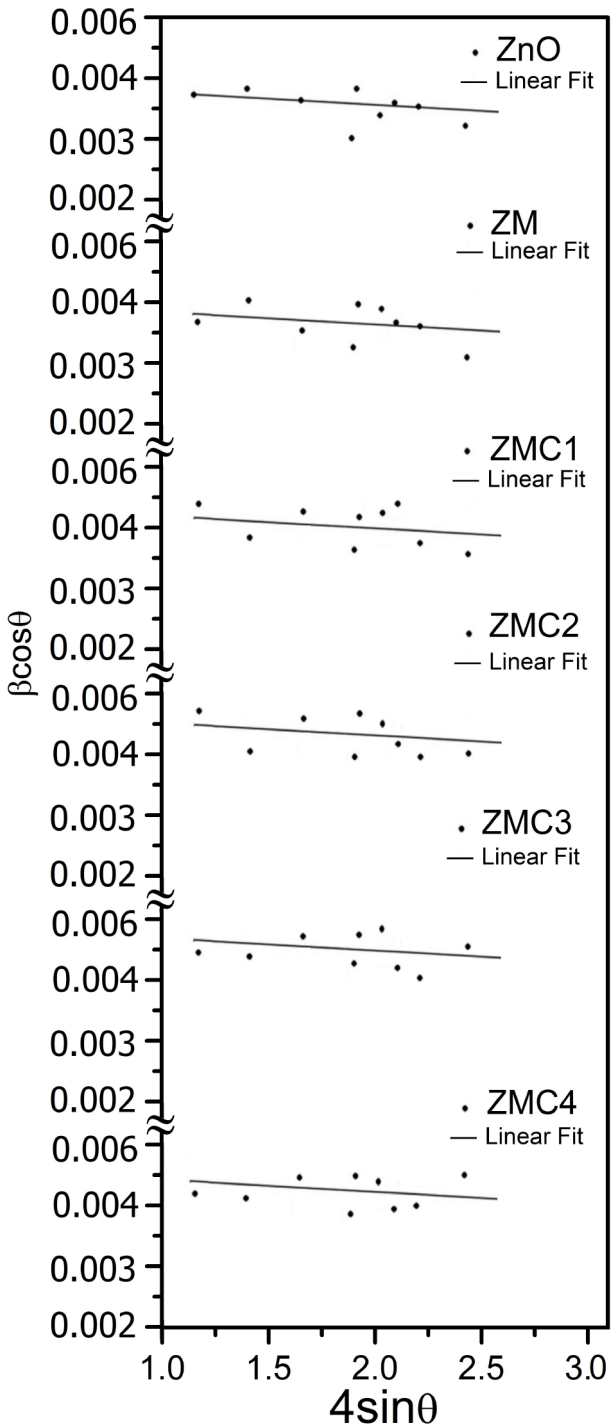

Fig. 2 Williamson-Hall analysis (UDM plot) of bare and $Zn_{0.98}Mn_{0.02}Co_xO$ $(0.00 \leq x \leq 0.025)$ nanoparticles. ZnO and $Zn_{0.98}Mn_{0.02}Co_xO$ $(0.00 \leq x \leq 0.025)$

peaks of all nanoparticles. The crystalline size ($D_{(hkl)}$) and strain (ε) were calculated from the intercept of β_{hkl} cos θ axis and the slope of the linear fit respectively. The values of crystallite sizes ($D_{(hkl)}$) and strain $_{\epsilon}$ are listed in Table 1. It can be seen from the data, the strain in the co-doped ZnO is higher compared to the undoped ZnO. The strain value for undoped is 0.51×10^{-3}, whereas for co-doped ZnO it ranges from 0.53×10^{-3} to 0.65×10^{-3}. The increase in strain is attributed to the incorporation of dopants (Mn, Co,), which causes local alteration crystallographic defects [13]. The selected transmission electron micrograph images of pure ZnO (nanoparticles Z) and $Zn_{0.955}Mn_{0.02}Co_{0.025}O$ (nanoparticles ZMC4) nanoparticles are shown in Fig. 3. It can be seen from these figures that most of the nanoparticles are spherical in shape while few of them are faceted. Typical particle size ranges from 21 to 34 nm, which is consistent with the crystallite size estimated from XRD data. High-resolution TEM images are presented in the left insects of Fig. 3, which clearly depicted that the nanoparticles are highly crystalline in nature. The interplanar lattice spacing along the plane (002) is found to be 0.26 nm. The histogram of size distribution of FWHM is found to be 3.2 in both cases and is plotted in the right insets of Fig. 3.

X-ray photoemission spectroscopy was employed to identify the oxidation state of the dopant, which helps to rule out the possible occurrence of secondary phases. It can be possible to detect the tiny metallic cluster (if any) that has generally not been detected by XRD. All XPS spectra were calibrated by using a carbon (C_{1s}) peak (284 eV). Full survey scans of XPS spectra of selected nanoparticles (Z, ZM, and ZMC4) are shown in Fig. 4(a). In this measurement, our aim is to check whether the doped elements (Mn, Co) are incorporated successfully within ZnO matrix. A pair of most intense core level peaks of 1021.9 eV ($Zn2p_{3/2}$) and 1044.2 eV ($Zn2p_{1/2}$) correspond to cation (Zn) along with a core level at 530 eV (O1s) exhibits an anion (O) are dominantly observed in all survey scan. These core levels' binding energies correspond to the ZnO Wurtzite structure [14]. The XPS measurements further confirmed the dopants are in tetrahedral symmetry in the ZnO lattice. It can be seen from Fig. 4(a), the core level doublet peaks of Co and Mn appeared at 781.0 eV (Co $2p_{1/2}$), 796.8 eV (Co $2p_{3/2}$), and 641.6 (Mn $2p_{1/2}$), 653.4 ($Mn2p_{3/2}$) respectively. These core-level binding energies confirm that the dopants (Mn, Co) are in +2 oxidation states in the ZnO matrix [15]. In addition, doping concentration was also determined using XPS core analysis. The dopants' concertation is presented in Table 2. In order to check the existence of oxygen vacancies in the doped system as suggested by Carrettin et al. [16], representative oxygen core level spectra of Z and ZMC4 were analyzed. The data on the oxygen core level of both nanoparticles are shown in Fig. 4(b). It can clearly be seen that both representative oxygen core spectra show an asymmetric peak centered at 529.92 eV. The asymmetric peak was deconvoluted into three components using Shirley background and Voigt (mixed Lorentzian–Gaussian) function. The deconvoluted peaks at energies 529.9, 531.21, and 532.46 eV are referred

Content courtesy of Springer Nature, terms of use apply. Rights reserved.

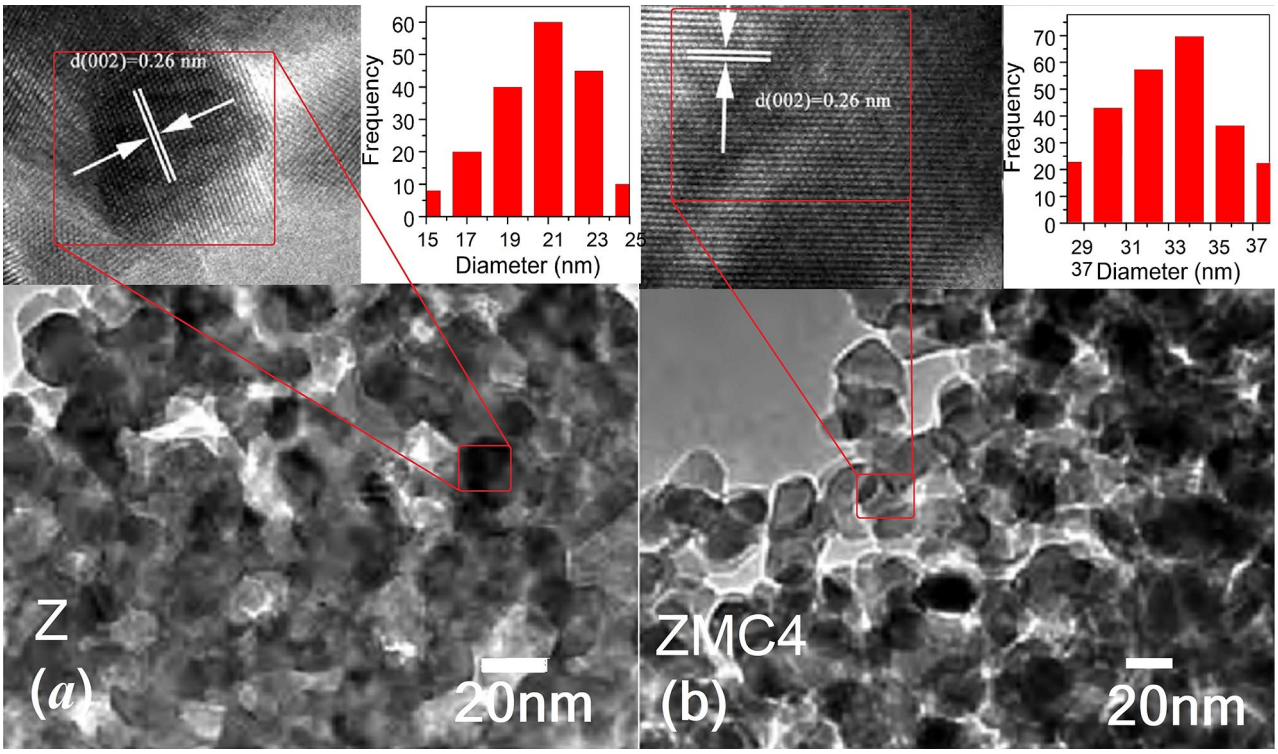

Fig. 3 TEM images of (**a**) bare ZnO nanoparticles (Z) and (**b**) $Zn_{0.955}Mn_{0.02}Co_{0.025}O$ nanoparticles (ZMC4). Left insets: HR-TEM images showing (002) crystalline planes. Right insets: size distribution histogram

to in the text as low binding energy component (LBEC: O_I), high binding energy component (HBEC: O_{II}), and O_{III} respectively. The peak of O_I is assigned to the lattice oxygen in the defect-free region (Zn−O). The peak of O_{III} and O_{II} represents the adsorption of oxygen species over the surface and oxygen vacancies regions respectively. As seen from Fig. 4(b) the intensity of oxygen core level (O_{II}), which represents oxygen vacancy, in ZMC4 nanoparticles is nearly double compared to nanoparticles Z. This clearly suggests the existence of a substantial amount of oxygen vacancy concentration in the doped system. The ratio of two oxygen vacancy components (O_{II} and O_I) can help to estimate the relative amount of oxygen vacancy concentration within the system [17]. The ratio O_{II}/O_I was found with the help of peak fitting analysis and the data is shown in Table 2. It is clear from Fig. 4(c) that there is an obvious increase in O_{II}/O_I from 0.35 to 0.64 with increasing doping concretion, suggesting the reasonable amount of oxygen vacancy concentration systematically increases with increasing dopants concentration. The increasing amount of oxygen vacancy concentration as a function of dopants (Mn, Co) could be understood as follows: when Mn ions are added, they may get substituted near the Co ions. The substitution of Co near Mn ions is possible because the Wurtzite crystal structure of ZnO is already distorted at the locations where Mn ions are present and thus it highly favors the formation of new defects within already distorted lattice. The formation energy of oxygen vacancy was theoretically found to be higher compared to the more perfect region of the lattice [18]. Therefore, increasing the concentration of oxygen vacancy as a function of dopants (Mn, Co) is well consistent. A threshold amount of oxygen vacancy in the magnetically doped semiconductor can help in mediating the exchange interaction between delocalized magnetic ions via free carriers, which will be discussed later. Our study further indicates that the dispersion of Mn and Co dopants within the ZnO matrix appears to follow a random pattern, particularly up to the annealing temperature of 600 °C. This observation is supported by the XPS core spectra of Mn2p and Co2p. The Mn 2p core level and the Co 2p core level are illustrated in Fig. 5. Notable peaks at 641.27 and 653.87 eV in the Mn 2p spectra correspond to the binding energies of Mn $2p_{3/2}$ and $2p_{1/2}$, while peaks at 781.5 and 797 eV in the Co 2p spectra are associated with the binding energies of Co $2p_{3/2}$ and $2p_{1/2}$. The binding energies and energy separations (12.6 eV and 15.6 eV) of these peaks suggest the presence of Mn^{2+} and Co^{2+} ions. It's noteworthy that for Co oxides and Mn oxides, the separation of binding energy is estimated to be 15.9 eV and 11.7 eV respectively, as reported in literature [19]. These findings support the successful incorporation of Mn^{2+} and Co^{2+} ions into the ZnO matrix. It's worth noting that the signal-to-noise ratio of the XPS spectra was affected

Content courtesy of Springer Nature, terms of use apply. Rights reserved.

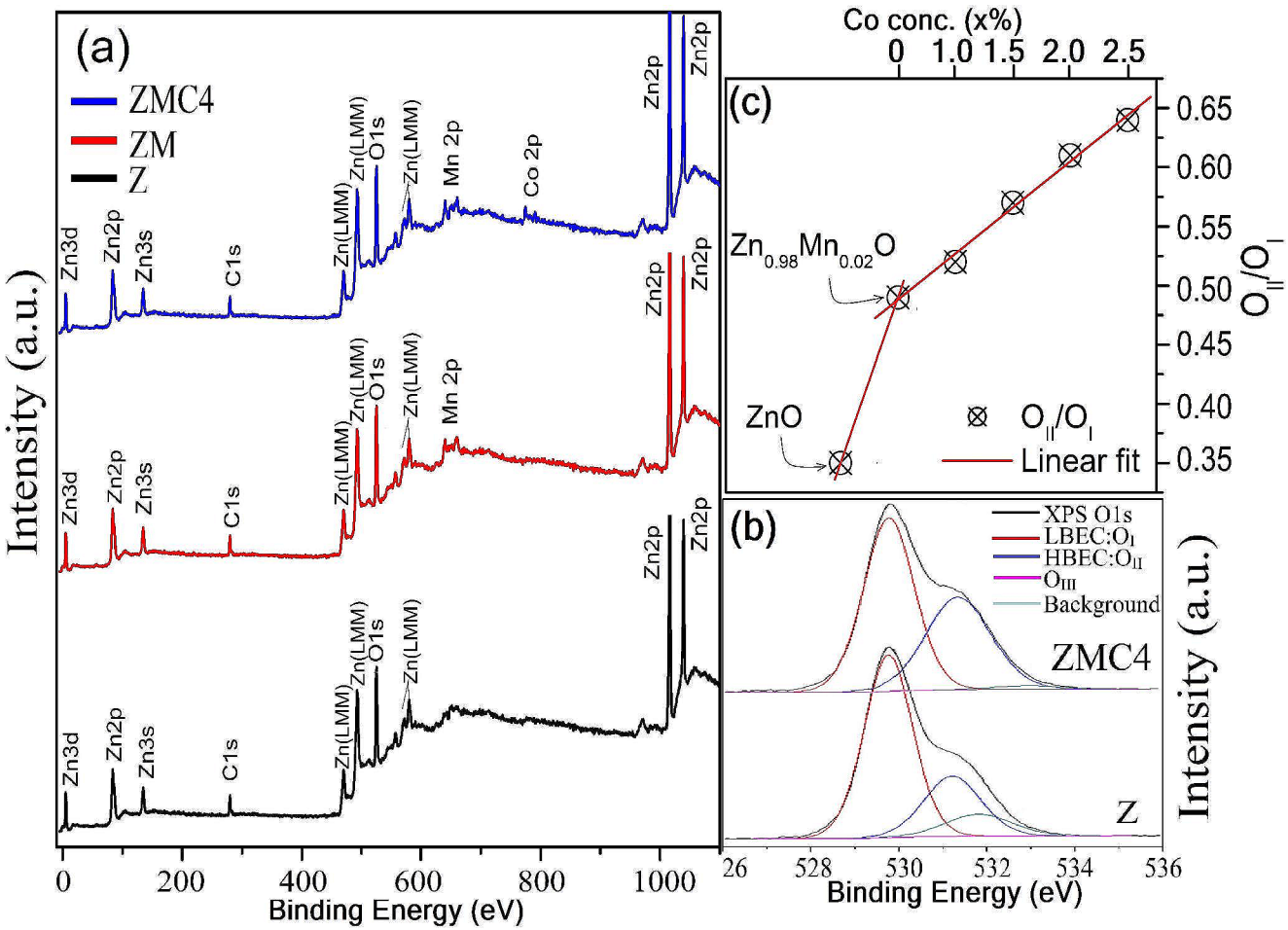

Fig. 4 (**a**) XPS spectra of raw data of samples Z, ZM, and ZMC4 (**b**) XPS O1s spectra of Z and ZMC4 (**c**) Plot of relative intensity of high binding energies versus cobalt concentration: Red show low binding energy component O_I (LBEC), blue show high binding energy component O_{II} (HBEC), pink show O_{III}

Table 2 Comparison of Concentration of Mn, Co and relative oxygen vacancies concentration (O_{II}/O_I) estimated from XPS analysis

#	Sample	Concentration		
		Mn%	Co%	O_{II}/O_I
1	Z	–	–	0.35
2	ZM	1.97	–	0.49
3	ZMC1	1.98	0.97	0.52
4	ZMC2	1.96	1.43	0.57
5	ZMC3	1.97	1.97	0.61
6	ZMC4	1.95	2.42	0.64

O_{II}: High binding energy component

O_I: High binding energy component

O_{II}:O_I: Corresponds to oxygen vacancy concentration

by the limited concentration of Mn^{2+} and Co^{2+} dopant ions, resulting from the low concentration of Mn and Co in the sample. Additionally, the Zn2p core spectra indicates that the two peaks correspond to $Zn2p_{3/2}$ and $Zn2p_{1/2}$ at binding energies of 1022.25 eV and 1045.30 eV, respectively. The difference between the peaks is measured to be 23.05 eV, consistent with literature findings, indicating the presence of the ZnO lattice. Analysis of the XPS Zn2p core spectra suggests that while the dopants introduce local defects, the overall structural integrity of the ZnO lattice remains unchanged.

The dielectric properties were explored by impedance spectroscopy in the frequency range of 40 to 10^6 Hz. In order to make the same shape and size of pellets, the standard hydraulic press with a pressure of 10 ton for 1 min was used. The nanoparticle pellet was then sandwiched between copper foil to attain a geometry of Cu/pellet/Cu. The standard silver paste was pasted on either side of the foil followed by joining a thin copper wire in turn to serve as good ohmic contact. The real part of the dielectric constant (ϵ') versus frequency of pure and (Mn, Co) co-doped ZnO nanoparticles at room temperature is depicted in Fig. 6. It can be seen from this figure that the dielectric constant lessens exponentially with the increase of frequency in all nanoparticles, confirming the entails of conducting grains

Content courtesy of Springer Nature, terms of use apply. Rights reserved.

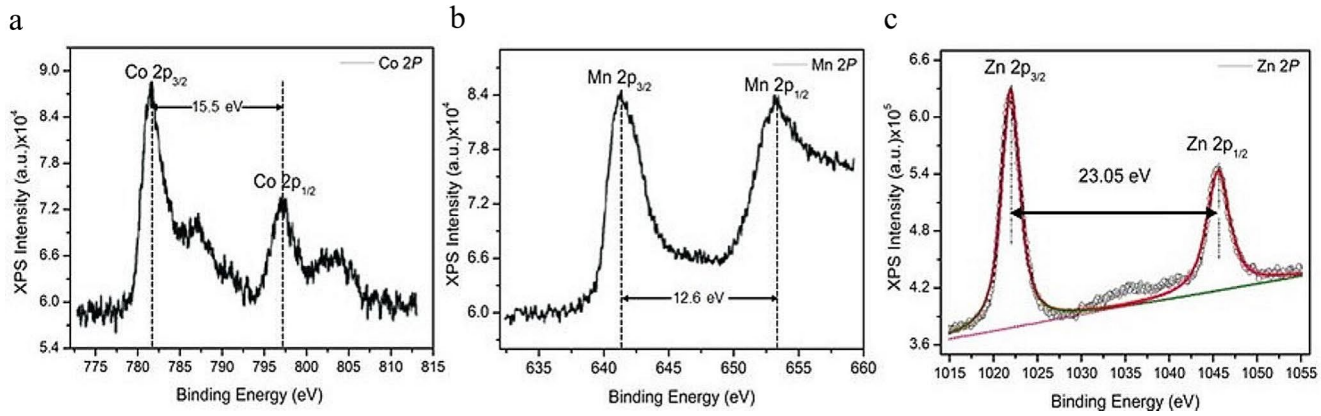

Fig. 5 (**a**) Co 2p and (**b**) Mn 2p and (c) Zn 2p core level XPS spectra of the ZMC4 nanoparticles. Black hollow dots show the XPS raw data, the red solid line corresponds to the envelope-fitting curve

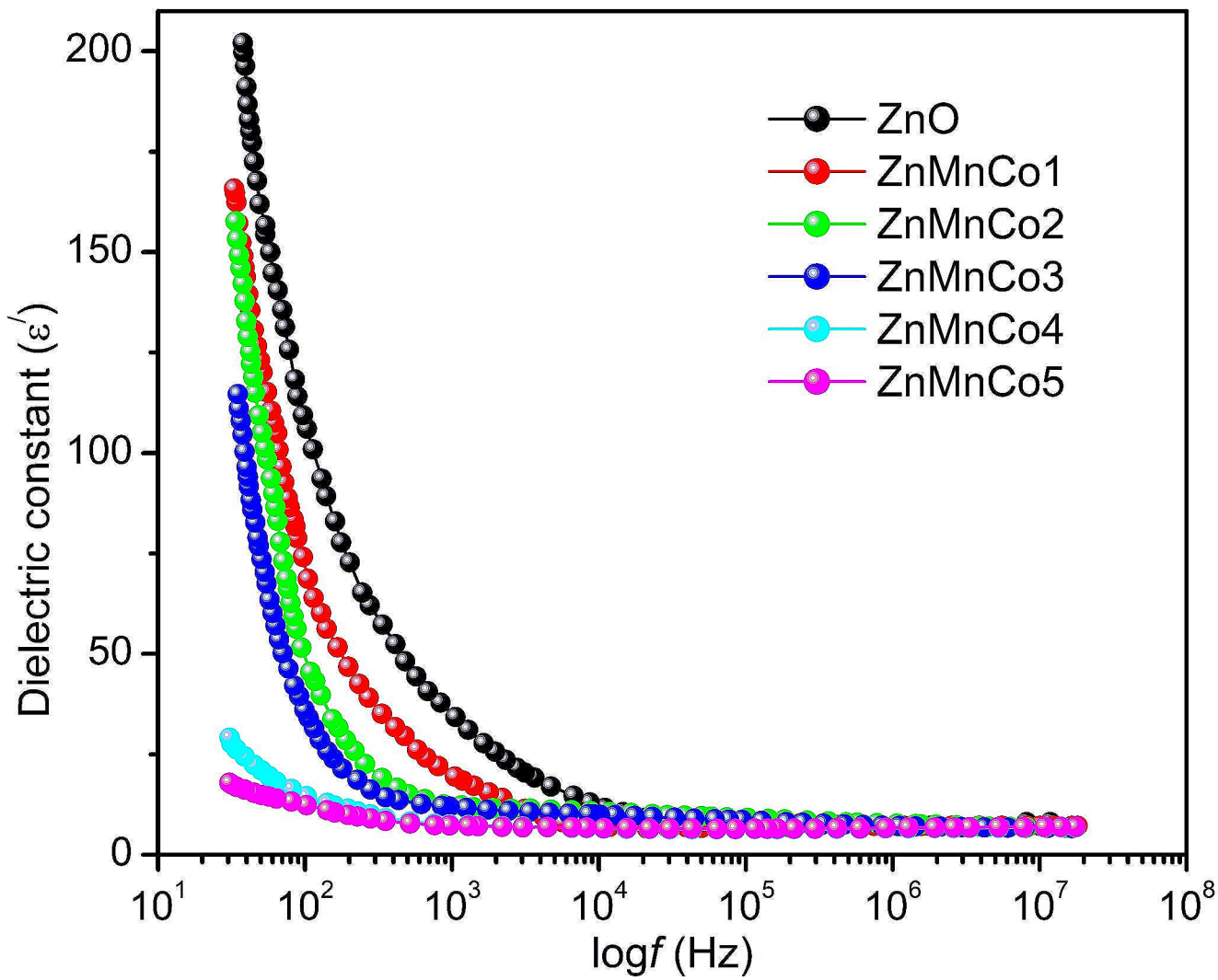

Fig. 6 Plot of dielectric constant versus frequency of bare ZnO and $Zn_{0.98}Mn_{0.02}Co_xO\,(0.00 \leq x \leq 0.025)$ at room temperature

Content courtesy of Springer Nature, terms of use apply. Rights reserved.

which estrangement by non-conducting grain boundaries. It is further depicted that the dielectric constant increases with increasing concentration of co-doped (Mn, Co). It can be clearly interpreted by the Maxwell-Wagner model, which generally refers to interfacial polarization occurring in electrically inhomogeneous systems. In the presence of an applied electric field charge carriers move through interfaces between two grains and thus pile up at the grain boundary and give rise to a Debye-like relaxation. Such relaxation leads to enhance polarization, resulting in a higher value of a dielectric constant [20]. In addition to the Maxwell-Wagner model, the dielectric constant at lower frequencies could also be a function of the polarization of charge accumulated at the interface, vacancy-related defects, and unsaturated bonds [21]. In the previous section, we successfully argued that the reasonable amount of oxygen vacancy concentration systematically increases with increasing dopant (Mn, Co) concentration. The surplus amount of oxygen vacancies could trap charge carriers, hence imposing a large polarization in the system, which leads to enhance low-frequency dielectric constant. Furthermore, Fig. 6 reveals that the dielectric constant decreases with the increased frequency for all the nanoparticles. An exponentially decreasing trend in dielectric constant is observed at lower frequency region. However, the change in dielectric constant becomes slower at high frequency, leading to an independent frequency trend. The rapid decrease in dielectric constant with an increase in frequency is obvious behaviour for metallic oxide insulating nanoparticles [22].

Room temperature magnetization curves M(H) of nanoparticles Z and ZM are shown in Fig. 7(a). It is evident from the figure that the pure ZnO nanoparticle (nanoparticles Z) is diamagnetic while Mn-doped ZnO (nanoparticles ZM) exhibits an s-shaped hysteresis loop with a very small coercive field 56Oe at room temperature. The diamagnetic behavior of pure ZnO at room temperature agrees with the literature [23]. Nevertheless, the non-zero magnetic moment and coercive field of ZM nanoparticle at the reduced field (H/T) depicts non-zero value as clearly shown in the right inset of Fig. 7(a). Sharma et al. reported the weak remnant magnetization and coercive field at room temperature suggests the existence of a mixed magnetic phase in Mn-doped ZnO nanoparticles [24]. The temperature dependence magnetization measurements were performed with two different configurations (*i*) field cooled (FC) and (*ii*) zero field cooled (ZFC) temperature dependence magnetization plot at $H = 500Oe$ is shown in the left inset of Fig. 7(a). The FC magnetization plot was fitted by the following equation [24].

$$M = M_o\left(1 - aT^{3/2}\right) + \frac{HC_1}{T} + \frac{HC_2}{T+\theta}$$

The last term contains a parameter 'θ' *that* represents Curie-Weiss temperature, and two constants C_1 and C_2 correspond to Curie law and Curie-Weiss law respectively, while exchange interaction represents as '*a*'. The first term in the equation corresponds to the spin-wave model. The second term represents the Curie law of the paramagnetic phase, and the third term represents the Curie–Weiss law of the antiferromagnetic phase. It can be seen from the left inset of Fig. 7(a), the FC magnetization data can be well-fitted with the above equation, revealing mixed magnetic phases in the ZM nanoparticles. The fitting parameters a, C_1, C_2, M_o, *and* θ are presented in Table 3. These parameters clearly suggest a mixture of magnetic phases exists with a

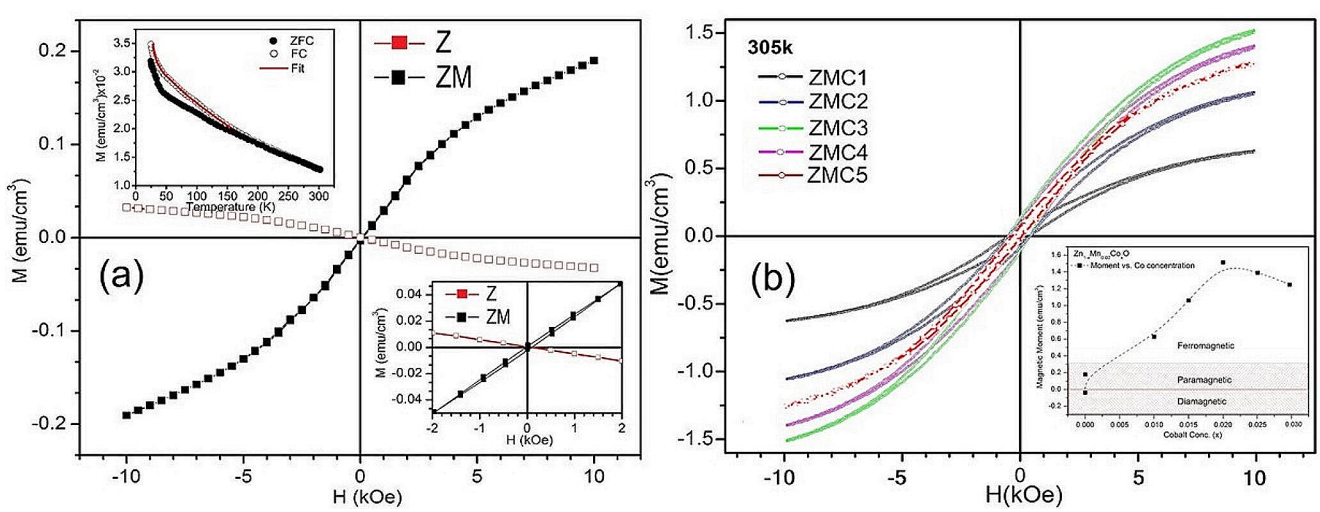

Fig. 7 (**a**) Magnetization versus magnetic field M(H) hysteresis loops of Z and ZM nanoparticles at room temperature. Right insets: M(H) loops of Z and ZM nanoparticles at reduced field (H/T). Left insets: FC and ZFC curves of ZM nanoparticles (**b**) M(H) hysteresis loops of $Zn_{0.98}Mn_{0.02}Co_xO\,(0.010 \le x \le 0.030)$. Inset: plot of magnetization versus Co concentration at 305k

Content courtesy of Springer Nature, terms of use apply. Rights reserved.

Table 3 Magnetization (M), Remanent magnetization (Mr) and Coercive field (Hc) values for $Zn_{0.98}Mn_{0.02}Co_xO\,(0.010 \leq x \leq 0.025)$

$a(K)^{\frac{2}{3}}$	$C_1(emuKg^{-1}Oe^{-1})$	$C_2(emuKg^{-1}Oe^{-1})$	$M_o\left(\frac{emu}{g}\right)$	$\theta\,(K)$
1.32×10^{-4}	2.48×10^{-5}	0.026	0.0016	−320
No.	**Sample**	**M (emu/cm^3)**	**M_r(emu/cm^3)**	**H_C(kOe)**
1.	Z	-	-	-
2.	ZM	-	-	-
3.	ZMC1	0.63	0.056	235
4.	ZMC2	1.06	0.096	234
5.	ZMC3	1.52	0.137	232
6.	ZMC4	1.39	0.127	233

Data obtained from fitting of FC magnetization plot of ZM Nonoparticles

predominantly ferromagnetic fraction (M_o). This supports a weak but s-shaped magnetic hysteresis given in the main frame of Fig. 7(a). The room temperature magnetic moment at 10 kOe is found to be ~0.02 μ_B/Mn (0.19 emu/cm^3) for ZM nanoparticles. A very small value of magnetic moment compared to the theoretically reported value of 5 μ_B/Mn for a free Mn^{+2} ion, confirms the existence of a fraction of Mn^{2+} ions contributing to the observed ferromagnetism. A small contribution of Mn dopant in the overall ferromagnetic moment could be attributed to the simultaneous manifestation of multiple competing interactions such as ferromagnetic, paramagnetic, and antiferromagnetic ordering in the ZM nanoparticles [25]. The field-dependent magnetization curves of mixed dopant nanoparticles namely ZCM1, ZCM2, ZCM3, ZCM4, and ZCM5 were measured at 305 K. The magnetization curves are plotted in Fig. 7(b). The corresponding values of magnetization (M_s) at 10kOe, remanence magnetization (M_r), and coercive field (H_c) for the nanoparticles for different cobalt concentrations at 305 K are presented in Table 3. Magnetization curves depict a clear non-zero M_r and H_C suggesting the existence of a ferromagnetic component. All magnetization curves follow a nearly S-shape and linear dependence with an applied magnetic field. Furthermore, all magnetization curves do not saturate even at an applied magnetic field of 10 kOe. The tendency of the unsaturated magnetic moment even at a higher applied magnetic field suggests the existence of competition between predominantly ferromagnetic and weak antiferromagnetic components. Such competition interaction within mixed magnetic phases was previously reported in some literature [26]. The magnetic moments are found to be increased with increasing Co concentration from 0.63 emu/cm^3 (ZMC1) to 1.52 emu/cm^3 (ZMC3). However, it starts to marginally decrease at a higher concentration of Co (ZMC4 and ZMC5). The above-cited interaction between mixed magnetic phases might be switched over toward the dominant antiferromagnetic phase at a higher Co concentration and thereby dipping the ferromagnetic moment to 1.39 emu/cm^3. Finally, now we focus on the possible origin of ferromagnetic ordering in our nanoparticles (ZMC1, ZMC2, and ZMC3) considering the theoretically proposed model. The ferromagnetism was reported in Mn/Co co-doped ZnO via oxygen vacancies [27]. Our results, containing (Mn/Co-doped ZnO and oxygen vacancies), are also consistent with the reported literature on the mechanism such as the spin-split-impurity band [28]. The fundamental requirement of this model is to transfer charge from a donor-impurity band to an unoccupied localized state (3d in our case) near a Fermi level. Our results revealed that only Mn-doped ZnO nanoparticle exhibits superparamagnetic behavior while Mn/Co co-doped ZnO nanoparticle depicts relatively significant ferromagnetic ordering. It recalls from the above-cited ferromagnetic model, the relative value of ferromagnetic ordering strongly depends upon the location of 3d states within the band gap. For a given d-element having a different 3d state, the strength of hybridization between the spin-split impurity band and 3d state would be different. This would surely lead to different strengths of hybridization and net magnetic ordering. For an Mn dopant, the donner impurity states and 3d spin-down state are located relatively far away, thereby disappearing magnetic ordering. However, for Co dopant the hybridization of aforesaid 3d states with donor impurity band is strong enough resulting in a strong ferromagnetic ordering [24]. At this point we can argue that in the case of Mn/Co co-doped ZnO nanoparticles, the Fermi level is situated close to a center of the density of states and therefor ferromagnetic appears via the well-known Stoner criterion $N(E_f).j \sim 1$, where $N(E_f)$ is a density of states near Fermi level and J is magnetic exchange interaction factor. We can conclude that our results are, at least qualitatively explained by Coey's extended model for nanoparticles [29].

4 Conclusion

ZnO and $Zn_{0.98}Mn_{0.02}Co_xO$ ($0.00 \leq x \leq 0.025$) nanoparticles were synthesized via sol-gel. XRD measurements confirmed pure hexagonal Wurtzite ZnO structure, with no Co- or Mn-related phases detected. XPS revealed oxygen vacancies crucial for room temperature ferromagnetic interaction

Content courtesy of Springer Nature, terms of use apply. Rights reserved.

stabilization. Magnetization measurements exhibited non-zero remanent magnetization and coercivity, indicating a weak ferromagnetic ordering. Magnetic moments increased with Co concentration, peaking at 1.52 emu/cm³ for ZMC3, then slightly decreased to 1.39 emu/cm³ for higher Co concentrations, possibly indicating a shift towards antiferromagnetic dominance. Complex magnetic behavior in $Zn_{0.98}Mn_{0.02}Co_xO$ reflects mixed magnetic phases and competing ferromagnetic and antiferromagnetic interactions.

Acknowledgements The work at Nanoscale Research Laboratory, Department of Physics University of Karachi partially supported by the Deans Research Grant 2021-22 under the Karachi University Research Program (KURP).

Author contributions Wafa Gul, Sadaf Qaseem, and Zuhoor Elahi equally contributed to the conceptualization of research problems and the development of the methodology. They designed the experimental setup and conducted the characterization of the (Mn, Co) doped ZnO nanoparticles. M. Naeem and M. Ikram were extensively involved in the analysis and interpretation of the experimental data. Their contributions were particularly aligned with the existing theoretical model of room temperature ferromagnetic ordering in diluted magnetic semiconductor (DMS) systems. All authors participated in joint meetings where the research idea, methodology, and data interpretation were discussed. The manuscript was collectively prepared by all authors, with each providing critical feedback and revisions.

Data availability The datasets generated and analyzed during the current study are available from the corresponding author upon reasonable request. Raw data supporting the findings of this study are stored securely and will be made available in accordance with the journal's policies and guidelines.

Declarations

Conflict of interest We wish to confirm that there are no known conflicts of interest associated with this publication and there has been no significant financial support for this work that could have influenced its outcome.

References

1. J.W. Lu, E. Chen, M. Kabir, M.R. Stan, S.A. Wolf, Int. Mater. Rev. **61**, 456–472 (2016)
2. D.D. Awschalom, E.F. Michael, Nat. Phys. **3**, 153–159 (2007)
3. T. Dietl, H. Ohno, F. Matsukura, J. Cibert, E D Ferrand. **287**, 1019–1022 (2000)
4. H. Morkoç, O. Umit, Wiley, (2008)
5. R.B. Narzary, R.N.S. Dey, A. Mondal, G. Bouzerar, K. Manoranjan, S. Ravi, S.K. Srivastava, J. Alloys Compd. **934**, 167874 (2023)
6. I.K. Kuryliszyn, W. Dobrowolski, M. Arciszewska, N. Romčević, M. Romčević, B. Hadžić, D. Sibera, U. Narkiewicz, Phys. E: Low-dimensional Syst. Nanostruct. **98**, 10–16 (2018)
7. D.S. Birajdara, R.C. Alangeb, S.D. Morec, V.D. Murumkard, K.M. Jadhave, Des. Eng. **2351**, 9789 (2018)
8. M. Naeem, S.K. Hasanain, J. Phys.: Condens. Matter. **24**, 245305 (2012)
9. K. Omri, E.G. Jaber, O.M. Lemine, M. Bououdina, Z. Bei, E.M. Lassaad, Superlattices Microstruct. **60**, 139–147 (2013)
10. A. Kumari, A. Kumar, R. Dawn, J. Roy, S. Jena, R. Vinjamuri, D. Panda, S.K. Sahoo, V.K. Verma, S. Mahapatra, A. Rahaman, A. Ahlawat, M. Gupta, K. Kumar, A. Kandasami, V.R. Singh, J. Alloys Compd. **933**, 167739 (2023)
11. J. Wojnarowicz, K. Sylwia, C. Tadeusz, G. Stanislaw, L. Witold, K. Wojciech, I. Malgorzata, I. Lukasiewicz, Beilstein journal of nanotechnology 6 (2015) 1957
12. Y. Caglar, J. Alloys Compd. **560**, 181 (2013)
13. G. Vijayaprasath, R. Murugan, S. Asaithambi, G. AnandhaBabu, P. Sakthivel, T. Mahalingam, Y. Hayakawa, G. Rav, Appl. Phys. A **122**, 122 (2016)
14. J.F. Moulder, W.F. Stickle, P.E. Sobol, K.D. Bomben, Eden Prairie, MN: Perkin-Elmer Corporation). (1992)
15. L. Wei, W. Guojing, C. Chienhua, L. Jiecui, L. Zhengcao, Nanomaterials. **1**, 20 (2017)
16. C. Silvio, H. Yalin, A.G. Veronica, C.G. Bruce, T. Susana, J.C. Jose, C Avelino Chemistry–A Eur. J. **27**, 7771–7779 (2007)
17. M. Naeem, S.K. Hasanain, M. Kobayashi, Y. Ishida, A. Fujimori, S. Buzby, and S. Ismat Shah, Nanotechnology 17 (2006) 2675
18. O. Fumiyasu, C. Minseok, T. Atsushi, S. Atsuto, T. Isao, J. Phys.: Condens. Matter. **22**, 384211 (2010)
19. Pulse Electrodeposition of Manganese Oxide for High-Rate Capability Supercapacitors, F. Xiao, Y. Xu, Int. J. Electrochem. Sci., **7**, 7440–7450, (2012)
20. M.M.N. Ansari, A. Quddus, S. Khan Materials Today: Proceedings (2023)
21. D. Kaur, B. Amardeep, S. Tripti, M Charu Int. J. Opt. **2021**, 1–20 (2021)
22. A. Safeen, S. Kashif, M. Shafique, Y. Iqbal, N. Ahmed, M.A.R. Khan, G Asghar RSC Adv. **12**, 11923–11932 (2022)
23. S. Zhou, K. Potzger, J. Von Borany, R. Grötzschel, W. Skorupa, M. Helm, J. Fassbender, Phys. Rev. B **77**, 035209 (2008)
24. V.K. Sharma, M. Najim, A.K. Srivastava, G.D. Varma, J. Magn. Magn. Mater. **324**, 683–689 (2012)
25. Z.L. Lu, W. Miao, W.Q. Zou, M.X. Xu, F.M. Zhang, J. Alloy Compd. **494**, 392–395 (2010)
26. Y. Köseoğlu, J. Magn. Magn. Mater. **373**, 195–199 (2015)
27. X.H. Xu, H.J. Blythe, M. Ziese, A.J. Behan, J.R. Neal, A. Mokhtari, R.M. Ibrahim, A.M. Fox, G Gehring New. J. Phys. **8**, 135 (2006)
28. K.W. Nielsen, J.B. Phillip, M. Opel, A. Erb, J. Simon, L. Alff, R. Gross, Superlattices Microstruct. **37**, 327 (2005)
29. J.M. Coey, K. Wongsaprom, J. Alaria, M. Venkatesan, J. Phys. D: Appl. Phys. **41**, 134012 (2008)

Publisher's Note Springer Nature remains neutral with regard to jurisdictional claims in published maps and institutional affiliations.

Springer Nature or its licensor (e.g. a society or other partner) holds exclusive rights to this article under a publishing agreement with the author(s) or other rightsholder(s); author self-archiving of the accepted manuscript version of this article is solely governed by the terms of such publishing agreement and applicable law.

Content courtesy of Springer Nature, terms of use apply. Rights reserved.

Terms and Conditions

Springer Nature journal content, brought to you courtesy of Springer Nature Customer Service Center GmbH ("Springer Nature").

Springer Nature supports a reasonable amount of sharing of research papers by authors, subscribers and authorised users ("Users"), for small-scale personal, non-commercial use provided that all copyright, trade and service marks and other proprietary notices are maintained. By accessing, sharing, receiving or otherwise using the Springer Nature journal content you agree to these terms of use ("Terms"). For these purposes, Springer Nature considers academic use (by researchers and students) to be non-commercial.

These Terms are supplementary and will apply in addition to any applicable website terms and conditions, a relevant site licence or a personal subscription. These Terms will prevail over any conflict or ambiguity with regards to the relevant terms, a site licence or a personal subscription (to the extent of the conflict or ambiguity only). For Creative Commons-licensed articles, the terms of the Creative Commons license used will apply.

We collect and use personal data to provide access to the Springer Nature journal content. We may also use these personal data internally within ResearchGate and Springer Nature and as agreed share it, in an anonymised way, for purposes of tracking, analysis and reporting. We will not otherwise disclose your personal data outside the ResearchGate or the Springer Nature group of companies unless we have your permission as detailed in the Privacy Policy.

While Users may use the Springer Nature journal content for small scale, personal non-commercial use, it is important to note that Users may not:

1. use such content for the purpose of providing other users with access on a regular or large scale basis or as a means to circumvent access control;
2. use such content where to do so would be considered a criminal or statutory offence in any jurisdiction, or gives rise to civil liability, or is otherwise unlawful;
3. falsely or misleadingly imply or suggest endorsement, approval , sponsorship, or association unless explicitly agreed to by Springer Nature in writing;
4. use bots or other automated methods to access the content or redirect messages
5. override any security feature or exclusionary protocol; or
6. share the content in order to create substitute for Springer Nature products or services or a systematic database of Springer Nature journal content.

In line with the restriction against commercial use, Springer Nature does not permit the creation of a product or service that creates revenue, royalties, rent or income from our content or its inclusion as part of a paid for service or for other commercial gain. Springer Nature journal content cannot be used for inter-library loans and librarians may not upload Springer Nature journal content on a large scale into their, or any other, institutional repository.

These terms of use are reviewed regularly and may be amended at any time. Springer Nature is not obligated to publish any information or content on this website and may remove it or features or functionality at our sole discretion, at any time with or without notice. Springer Nature may revoke this licence to you at any time and remove access to any copies of the Springer Nature journal content which have been saved.

To the fullest extent permitted by law, Springer Nature makes no warranties, representations or guarantees to Users, either express or implied with respect to the Springer nature journal content and all parties disclaim and waive any implied warranties or warranties imposed by law, including merchantability or fitness for any particular purpose.

Please note that these rights do not automatically extend to content, data or other material published by Springer Nature that may be licensed from third parties.

If you would like to use or distribute our Springer Nature journal content to a wider audience or on a regular basis or in any other manner not expressly permitted by these Terms, please contact Springer Nature at

onlineservice@springernature.com